ICAS 2020 SHANGHAI
International Council of the Aeronautical Sciences
32nd Congress of the International Council of the Aeronautical Sciences
September 6-10, 2021
Pudong Shangri-La, Shanghai, China

Natural-Laminar-Flow Airfoil Design Optimization Considering Crossflow Instability When Configured on a Swept Wing

Zhen-Ming Xu[1], Zhong-Hua Han[1*], & Wen-Ping Song[1]

[1]Institute of Aerodynamic and Multidisciplinary Design Optimization,
National Key Laboratory of Science and Technology on Aerodynamic Design and Research,
School of Aeronautics, Northwestern Polytechnical University,
Xi'an, 710072, P. R. China

Abstract

This paper proposes a novel design optimization method for transonic natural-laminar-flow (NLF) airfoils allowing for suppressing crossflow instability (CFI) when configured on a three-dimensional (3-D) swept wing. The distribution of the nondimensionalized crossflow pressure gradient (CFPG), a newly proposed flow parameter by the authors, is used as the objective flow characteristics related to crossflow in the corresponding 3-D case and combined with the total drag as the weighted objective function. The flow field and transition location are obtained by an extensively verified Reynolds averaged Navier-Stokes equations flow solver coupled an e^N method based on the linear stability theory. A surrogate-based optimization framework with Kriging model and parallel infill-sampling method is used to solve the optimization problem. The proposed method is demonstrated by the design optimization of a transonic NLF airfoil named NPU-LSC-72613, which is assumed to be configured on an infinite wing with a 30 deg sweep angle. Damped CFI and extensive laminar flow are obtained on the wing's upper surface, which demonstrates the feasibility of using the nondimensionalized CFPG to enable a 2-D NLF airfoil design optimization considering 3-D effects of crossflow.

Keywords: natural laminar flow, crossflow instability, design optimization

1. Introduction

Laminar flow has a great potential in viscous drag reduction in aerodynamics, which has become a key technology for environmentally responsible commercial aviation. To obtain extensive laminar flow on the wing of a transport aircraft, three methods are mainly used, namely natural laminar flow (NLF), laminar flow control (LFC), and hybrid laminar flow control (HLFC). Because NLF extends laminar flow through aerodynamic shape modifying, no extra energy and weight are expended. Besides, the flow mechanism obtained from the research of NLF can also assist the development of LFC and HLFC. As a result, many publications have paid much attention to NLF, as well as present paper.

A Low turbulence environment and weak freestream disturbances are generally accepted as the flight condition for transport aircraft [1]. Therefore, the small disturbances will suffer sufficient linear growth, rapid nonlinear growth, and then breakdown to turbulence. Because the linear growth stage is the central part and dominates the final transition location in this process, this paper only considers the linear growth of the small disturbances. For a two-dimensional (2-D) airfoil, the mainly instability mechanism is the Tollmien-Schlichting instability (TSI), which can be suppressed by a favourable pressure gradient in the mid-chord region. Once the airfoil is configured on a swept wing, two different instability mechanisms should be considered and even dominate the transition location. One is the

crossflow instability (CFI), which is destabilized by both favourable pressure gradients and adverse pressure gradients. The other is the attachment-line transition (ALT), which can be controlled by a suitable leading-edge radius. Obviously, the challenge in the aerodynamic shape design of transonic NLF wings consists in compromising the requirements of stabilizing TSI and CFI as well as reducing wave drag.

For a transonic transport aircraft, the airfoils determine the primary aerodynamic performance of the wing. Therefore, it would be better to consider the requirements of NLF in the design of transonic airfoils. There are many successful examples for stabilizing TSI and obtaining extensive NLF, such as the NASA 6-series airfoil, the high-speed NASA HSNLF(1)-0213 airfoil and so on. However, it becomes more complicated when CFI is considered. It is natural to suppress CFI by modifying the pressure distribution. One feasible way is to arrange a small region of a zero or even adverse pressure gradient following a rapid leading-edge acceleration as done by Redeker et al. [2] and Campbell et al. [3]. This method even can be extended to the supersonic regime [4]. Additionally, because CFI is destabilized by three-dimensional (3-D) features, it is reasonable to consider more 3-D effects. In this respect, Streit et al. [5] developed a method based on sectional conical wings, which can consider the effects of wing sweep and taper without significantly increasing the computational efforts. A new flow parameter, called nondimensionalized crossflow pressure gradient (CFPG), is also proposed by Ref. [6]. The nondimensionalized CFPG can combine the effects of pressure distributions and wing sweep on crossflow as one parameter, which provides a different design objective for suppressing CFI.

The computational fluid dynamic (CFD) based design optimization methods have been widely used for transonic NLF airfoils. A representative method is the inverse design, which pursues the shape whose flow characteristics match well with the target. The successful applications of the inverse design method can be seen in Ref. [7-10]. The key of this method is the target flow characteristics depending on the experience of designers. In order to deeply explore the design space and gain the ability to handle multiple objectives and constraints, direct aerodynamic optimization methods have got rapid development. This method generally makes the design objective with the drag coefficient and searches a better point applying optimization algorithms. For example, gradient-based optimizations for NLF airfoils were demonstrated by Ref. [11-17], as well as the gradient-free methods were demonstrated by Ref. [18-21]. Although significant progress has been made in drag reduction and extending laminar flow, the direct aerodynamic shape optimization is regarded as a data-driven method that lacks the knowledge of designers. It may result in a useless aerodynamic shape. Recently, a hybrid inverse/optimization design method was proposed by Han et al. [22-24], which takes full advantages of both inverse design and direct optimization and has been successfully applied to single-point and multi-point design optimizations of transonic NLF airfoils.

Nevertheless, there is still a gap for the hybrid inverse/optimization design method to consider suppressing CFI for transonic NLF airfoils. The challenge is lied in finding suitable flow characteristics as a part of the design objective to connect with the flow mechanism of suppressing CFI. Suppose the chordwise pressure distribution is chosen as such flow characteristics. In that case, it may not be able to consider the 3-D features of CFI sufficiently, especially when the streamlines are highly curved. The curved streamlines are created by wing sweep combined with pressure gradients and then cause

crossflow inside the boundary layer. From this perspective, the nondimensionalized CFPG, which can consider the effects of both wing sweep and pressure distributions on crossflow, is supposed to provide a new solution for the target flow characteristics for the hybrid inverse/optimization design method. However, this idea still needs further verification, which motivates the research of this paper.

This paper proposes a design optimization method for transonic NLF airfoils, which enables the consideration of the CFI suppression in the corresponding 3-D swept wing, using the nondimensionalized CFPG. The presented design optimization method bases on the surrogate-based optimization framework and the hybrid inverse/optimization method. The distribution of a nondimensionalized CFPG is used as the objective flow characteristics and is combined with the total drag as the weighted objective function. The Reynolds averaged Navier-Stokes (RANS) flow solver features automatic transition prediction using the linear stability theory and the dual e^N method accounting for both TSI and CFI. A transonic NLF airfoil, which is assumed to be configured on an infinite wing with a 30 deg sweep angle, is used as the baseline. Then, numerical optimization is performed by the presented method to reduce the wave drag and to extend the laminar flow.

This paper continues in Section 2 with the description of the CFD solver, the optimization framework and the nondimensionalized CFPG. Section 3 presents the numerical optimization process of the transonic NLF airfoil. Section 4 gives the conclusions.

2. Methodology

2.1 Reynolds Averaged Navier-Stokes Equations Solver with Automatic Transition Prediction

An in-house flow solver, called PMNS2D, is used to simulate the steady, viscous flow over airfoils, which features automatic transition prediction based on the linear stability theory and e^N method. The PMNS2D code consists of a RANS solver, a boundary-layer solver, and a linear-stability analysis and transition prediction code.

The coupling of the RANS solver and the transition prediction module is shown in Figure 1. At first, the RANS equations are solved assuming a sufficient laminar flow region. The finite volume method and the central scheme are used for spatial discretization. The lower-upper symmetric Gauss-Seidel (LU-SGS) scheme is used for time integration. The Spalart-Allmaras one-equation model is used for turbulence closure. Besides, the multigrid and local-time stepping method are also used for convergence acceleration. Once the residual is below a threshold value, the iteration of solving the RANS equations is suspended, and the transition prediction is activated. The solved flow parameters at the outer edge of the boundary layer are transferred to the boundary-layer solver. The boundary-layer equations are solved in a non-orthogonal body-fitted coordinate system. The velocity profiles and temperature profiles as the inputs for the linear-stability analysis are obtained inside the boundary layer. Then, the linear-stability analysis code is executed, and the e^N method is used to calculate the amplification N factors of TSI and CFI, N_{TS} and N_{CF}. If any of the N_{TS} or N_{CF} exceeds the threshold value determined by experience and experiments, the laminar-to-turbulent transition is considered to take place. Finally, the predicted transition location is transferred back to the RANS solver, and the iteration is restarted. The process will repeat until both the transition location and the RANS equations solving are converged. Please note that an invariant flow is assumed in the spanwise direction to calculate the amplification of the CFI.

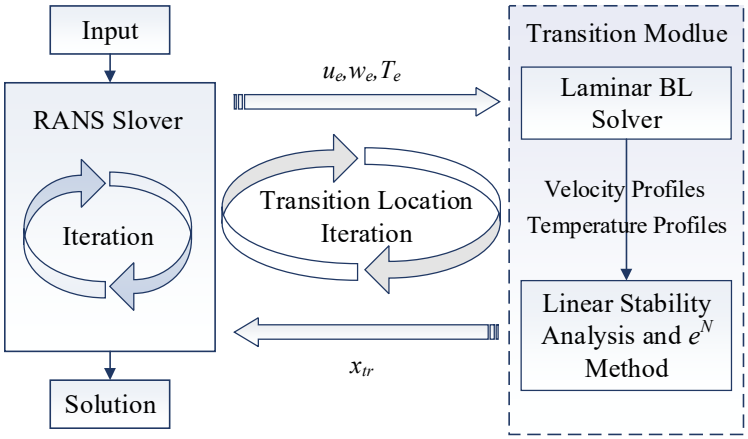

Figure 1 – Schematics of the coupling of the RANS solver and the transition prediction module

There are two simple test cases to verify the PMNS2D code with transition prediction, and other test cases can be referred to Ref. [20,21]. The first test case is the pressure-distribution simulation of the NASA HSNLF(1)-0213 airfoil, which is designed to obtain more than 55% and 65% laminar flow region at the upper and lower surface, respectively. The pressure distribution is simulated at the free flow condition of $Ma = 0.70, \mathrm{Re} = 4.0\times10^6, c_l = 0.26$ with free transition prediction, as depicted in Figure 2. The measured pressure distribution by experiment is from the Ref. [25], where the measured transition locations are not given at this flow condition. Therefore, there are only the calculated transition locations marked in Figure 2. A good agreement between the calculated pressure distribution and experimental data can be observed.

The second test case is the transition prediction of flow over the infinite swept wing configured with the NACA 64_2A015 airfoil. The sweep angle is 40 deg, and the flow condition is $Ma = 0.27, \alpha = -2.0^\circ$. The transition locations, CFI dominates, are predicted at different Reynolds numbers, as shown in Figure 3. The critical *N* factors, $[N_{TS}, N_{CF}]_{tr} = [10.5, 7.5]$, are based on experience. For all of these Reynolds numbers, a reasonably good agreement can be observed.

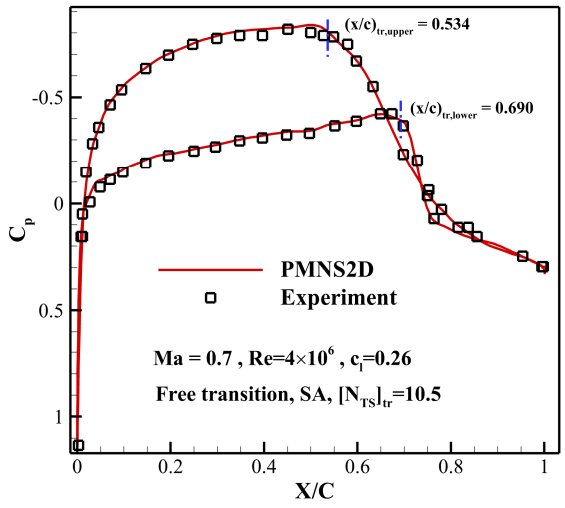

Figure 2 – Comparison of computed pressure distribution with the experimental data for the HSNLF-0213 airfoil at the flow condition of $Ma = 0.70, \mathrm{Re} = 4.0\times10^6, c_l = 0.26$

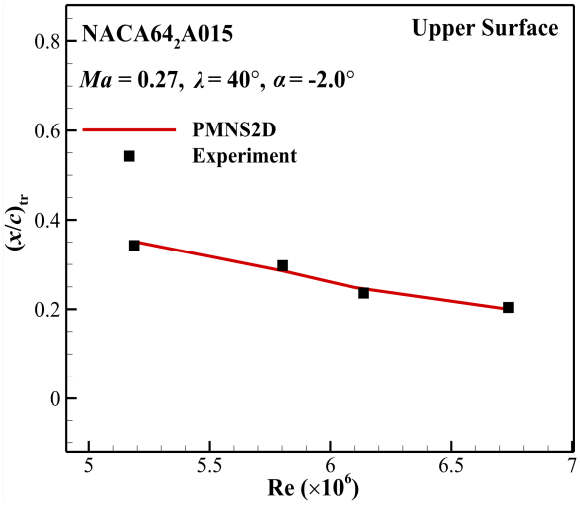

Figure 3 – Comparison of predicted transition locations with experimental data on the upper surface of the NACA64_2A015 airfoil at different Reynolds numbers

2.2 Nondimensionalized Crossflow Pressure Gradient[6]

The CFPG is such a pressure gradient that is aligned with the direction of crossflow (normal to inviscid streamlines) within the local tangent plane of the outer edge of the boundary layer. The dimensionless form can be written as

$$\left(\nabla p\right)_n^* \equiv \nabla p \bullet \sin\theta \Big/ \frac{\rho u^2}{L} \tag{1}$$

where the u is the velocity scale, the L is the length scale, and the ρ represents the density scale. The superscript "$*$" denotes dimensionless quantities. In this paper, the local inviscid flow velocity and density at the outer edge of the boundary layer are used as the velocity scale and density scale, respectively. The length scale is defined as

$$L = \sqrt{\frac{\nu_e x_c}{u_e}} \tag{2}$$

where the ν_e and u_e represent the kinematic viscosity and chordwise inviscid velocity at the outer edge of the boundary layer, and the x_c is the chord length.

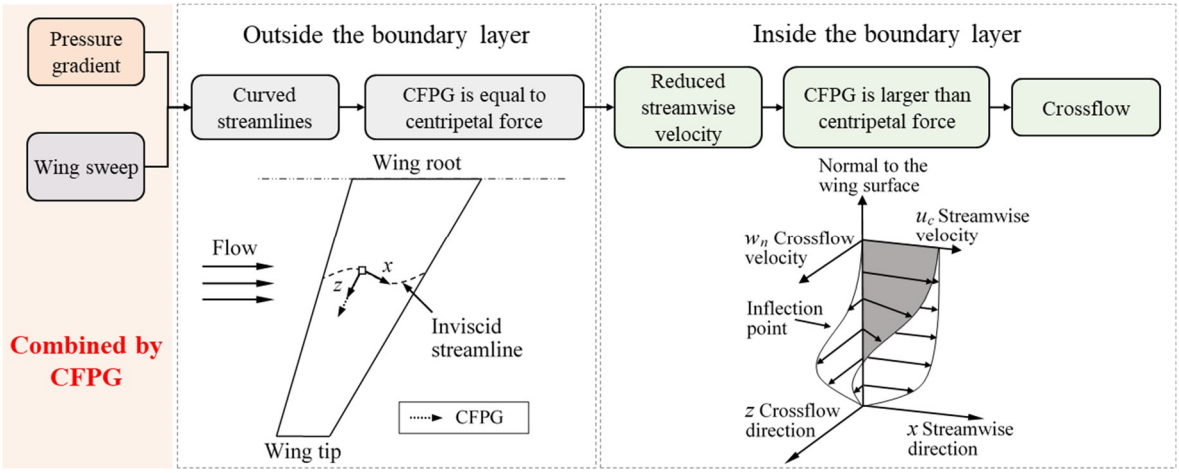

Figure 4 - Schematics of crossflow pressure gradient

The concept of nondimensionalized CFPGs is come from the generation process of crossflow, as shown in Figure 4. This process has been concluded by many papers such as Ref. [26]. Outside the boundary layer, wing sweep and pressure gradients create inviscid-flow streamlines in which CFPGs provide centripetal forces. Inside the boundary layer, streamwise velocities decrease towards the wing surface, but the CFPGs remain constant, which means the centripetal forces are larger than required. As a result, the streamlines become more and more curved towards the surface inside the boundary layer and then crossflow is formed. It can be seen that the crossflow is driven by the CFPG. The capability of the CFPG to combine the effects of wing sweep and pressure distributions has been demonstrated in Ref. [6].

2.3 Optimization Framework

The hybrid inverse/optimization design method combines the inverse design with the direct optimization to take full advantages of both methods. The inverse design objective is usually described as local flow characteristics. The direct optimization objective is usually a global parameter to deeply explore the design space. The general mathematical optimization problem can be represented as

$$\begin{aligned} \min \quad & obj = \omega_1 obj_{inv} + \omega_2 obj_{dir} \\ w.r.t. \quad & \boldsymbol{x} \in (\boldsymbol{x}_l, \boldsymbol{x}_u) \\ s.t. \quad & \begin{cases} h_p(\boldsymbol{x}) = 0 & p = 1,2,\cdots,N_p \\ g_m(\boldsymbol{x}) \geq 0 & m = 1,2,\cdots,N_m \end{cases} \end{aligned} \tag{3}$$

where the obj_{inv} and the obj_{dir} respectively denote the objective function of inverse design and direct optimization; the ω_1 and ω_2 are weight coefficients; the $\boldsymbol{x}$ represents the design variables with the upper bound $\boldsymbol{x}_u$ and the lower bound $\boldsymbol{x}_l$; the $h_p(\boldsymbol{x})$ and $g_m(\boldsymbol{x})$ denote the p-th equality constraint function and m-th inequality constraint respectively; and the numbers of equality and inequality constraints are represented by N_p and N_m. In the present paper, the inverse design objective is a part of nondimensionalized CFPG distribution at the leading edge, and the direct optimization objective is specified as the total drag. The flow chart of the optimization problem is plotted in Figure 5.

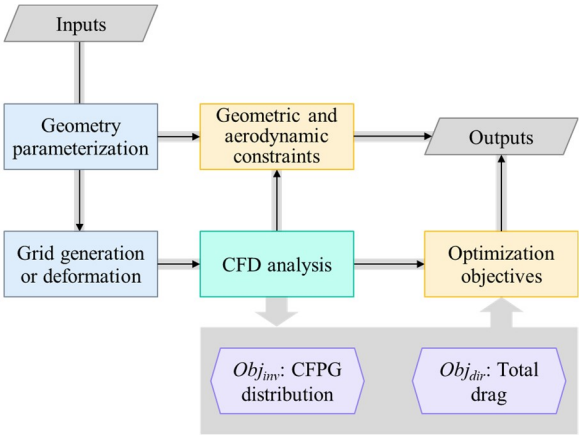

Figure 5 – Flow chart of the user-defined hybrid inverse/optimization design problem

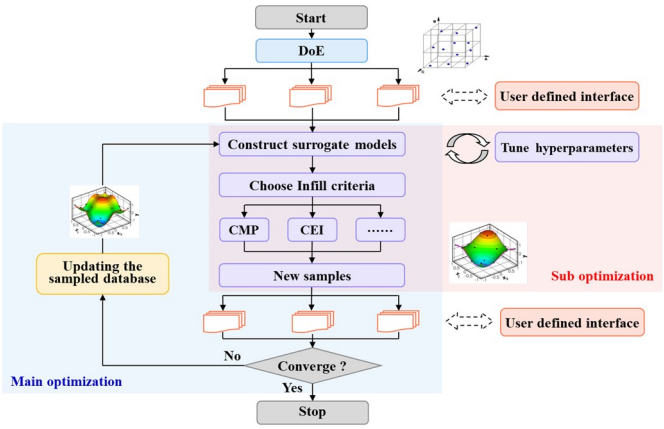

Figure 6 - Framework of the surrogate-based optimizer, SurroOpt

The optimizations are carried out using an in-house surrogate-based optimizer called SurroOpt. The framework of the optimizer is shown in Figure 6. A more detailed description of the SurroOpt code can be found in Ref. [27-31]. The steps to obtain an optimal airfoil are as follows. First, the Latin hypercube sampling method is used to choose the initial sample points in the modern design of experiments (DoE) process. Second, these initial points are transferred into the user-defined interface, such as shown in Figure 5, and the functional responses are transferred back to the main iteration. Third, initial Kriging surrogate models for the objective and constraint functions are modulated and built. Fourth, the parallel infill-sampling criteria and sub-optimizations based on the created Kriging surrogate models are used to find new sample points. Fifth, the newly added sample points are transferred into the user-defined interface, and the functional responses are obtained. Sixth, the newly added sample points and their functional responses are augmented to the sampled database to update the existed Kriging surrogate models. The steps from 4 to 6 are repeated until a termination criterion is activated.

3. Example

3.1 Initial Geometry

A transonic NLF airfoil, named NPU-LSC-72613, is used as the baseline. The airfoil and its pressure

distribution are shown in Figure 7. The aerodynamic performance of this airfoil at the flow condition of $Ma=0.72,\ Re_c=2.0\times10^7,\ c_l=0.6$ is shown in Table 1. The reference point for the pitching moment coefficient is at 0.25 x/c. The predicted transition location is the result considering both the TSI and CFI. It is worth noticing that a spanwise flow is assumed, which is equivalent to that on an infinite 30 deg swept wing, to calculate the amplification of the CFI. This operation leads to a Reynold number per unit chord

$$Re/C=\frac{\sqrt{u_c^2+w_s^2}}{\upsilon}\times1=\frac{u_c/\cos30^\circ}{\upsilon}\times1=\frac{Re_c}{\cos30^\circ}=2.31\times10^7 \tag{4}$$

for the stability analysis according to the cosine rule where u_c and w_s denote the chordwise and spanwise velocity. When any of the N_{TS} or N_{CF} exceed the critical values, $[N_{TS},N_{CF}]_{tr}=[9.5,6.5]$, the transition locations are determined and transferred back to the primary iteration.

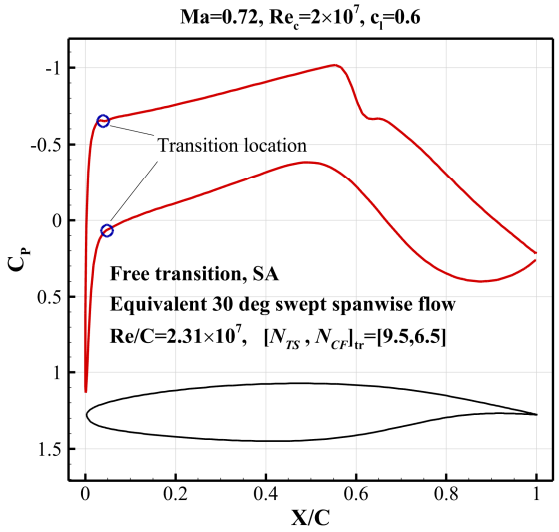

Figure 7 – Pressure distribution of the NPU-LSC-7613 airfoil with the predicted transition locations assuming a spanwise flow equivalent to 30 deg sweep angle

Table 1 – Aerodynamic and geometry properties of the NPU-LSC-72613 airfoil at the flow condition of $Ma=0.72,\ Re_c=2.0\times10^7,\ c_l=0.6$ with the predicted transition locations assuming a spanwise flow equivalent to 30 deg sweep angle

Airfoil	c_l	c_d (cts)	c_{df} (cts)	c_l/c_d	c_m	Transition location	*t/c*
NPU-LSC-72613	0.60	84.6	50.3	70.92	-0.124	The upper surface 4% The lower surface 5%	12.7%

3.2 Computational Grid

A series of structured grids with uniformly increasing size are generated for grid convergence study. The grid size of the coarse grid L3 is 185×73 in i (chordwise) and j (normal) direction. Then, the coarse grid is refined in both directions by a factor of two resulting in a medium grid L2 with the grid size 369×145. In the same way, a fine grid L1 with the grid size 737×289 is obtained. The sketches of these grids near the wall surface are shown in Figure 8.

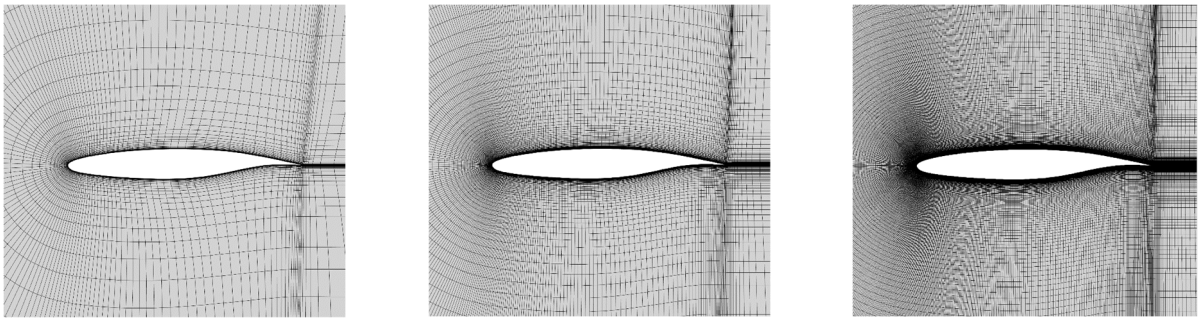

(a) Coarse grid L3 (b) Medium grid L2 (c) Fine grid L1

Figure 8 – Sketches of computational grids with different sizes

Table 2 - Comparison of drag coefficients (total and viscous) calculated in grids with different sizes

	Gird sizes	C_d (cts)	C_{df} (cts)
$h=0$	∞	37.74	25.14
L1	185×73	38.28	25.17
L2	369×145	39.91	25.26
L3	737×289	53.67	27.91

These grids are simulated at the flow condition of $Ma=0.72,\ Re_c=2.0\times10^7,\ c_l=0.6$. The lift coefficient is fixed at $c_l=0.6$. The calculated total and viscous drag coefficients in these grids are shown in Table 2, as well as the extrapolated drag coefficients in the zero-spacing grid (infinite grid). The grid convergence curves are plotted in Figure 9. The extrapolated values in the zero-spacing grid are obtained via Richardson extrapolation [32] of the results in the L1 and L2 grids. The values in Table 2 are presented in the form of drag counts, where one count represents 1×10^{-4}. It can be seen that the differences, 2.17 counts for total drag and 0.12 counts for viscous drag, between the L2 grid and the zero-spacing grid are acceptable, which compromise the precision and computation efforts. As a result, the L2 grid is used in the design optimization later.

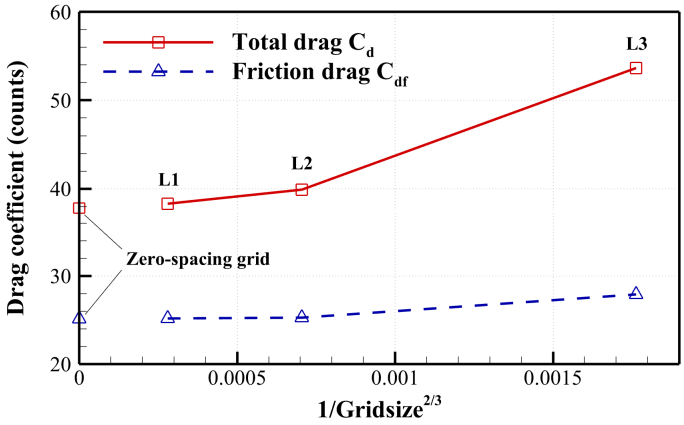

Figure 9 – Grid convergence curves for grids with different sizes

3.3 Hybrid inverse/optimization design of transonic NLF airfoil

The hybrid inverse/optimization design is performed to reduce the wave drag and to extend the laminar flow of the baseline airfoil with the equivalent 30 deg swept spanwise flow. The design point is specified as $Ma=0.72,\ Re_c=2.0\times10^7,\ c_l=0.6$, at which a strong shock wave can be observed. The

equivalent Reynold number per unit chord used for stability analysis is $Re/C = 2.31\times10^7$. The optimization is executed by SurroOpt code, and the aerodynamic performance is evaluated by PMNS2D code. The critical N factors for the TSI and CFI are specified as $\left[N_{TS}, N_{CF}\right]_{tr} = \left[9.5, 6.5\right]$ in the optimization process, which is slightly smaller than used in Sec. 2.1 to leave a safe margin. Free transition is only considered on the upper surface, and mandatory full turbulence is set on the lower surface. An eighth-order class function shape-function transformation (CST) method is used to disturb the baseline airfoil to get new shapes, which leads to 18 design variables.

The objective function contains a direct optimization objective and an inverse design objective. The direct optimization objective is specified as the total drag. The inverse design objective is generally determined based on the experience of designers. However, it is determined based on the characteristics of the nondimensionalized CFPG in the present paper. For example, the nondimensionalized CFPG distribution of the baseline airfoil with the equivalent 10 deg swept spanwise flow is used as the objective. The reason is that the nondimensionalized CFPG can combine the effects of wing sweep and pressure distribution on crossflow as one parameter, and a smaller sweep angle means more stabilized CFI. Thus, the nondimensionalized CFPG distribution of a smaller sweep angle is a natural inverse design objective for the pressure distribution optimization of a larger sweep angle to stabilize the CFI. Besides, there are also two constraints. The thickness/chord ratio of the airfoil is not allowed to decrease, and the absolute value of the pitching moment coefficient should be kept being smaller than that of the baseline airfoil. The mathematical model of the optimization is

$$\begin{aligned} \min \quad & obj = 0.3\bullet\frac{\sum\left|\left(\nabla p\right)_n^*\bullet Re_L - \left(\nabla p\right)_{n,target}^*\bullet Re_{L,target}\right|}{\sum\left|\left(\nabla p\right)_{n0}^*\bullet Re_{L0} - \left(\nabla p\right)_{n,target}^*\bullet Re_{L,target}\right|} + 0.7\bullet\frac{c_d}{c_{d0}} \\ w.r.t. \quad & \boldsymbol{x}\in\left(-0.02,\ 0.02\right) \\ s.t. \quad & (1)\ T/C \geq 12.7\% \\ & (2)\ \left|C_M\right| \leq \left|C_{M0}\right| \end{aligned} \tag{5}$$

where the Re_L denotes the local Reynolds number, and the subscript “0” refers to the baseline value. It is worth mentioning that only a small region of nondimensionalized CFPG, from the leading edge to $x/c = 0.07$, is used as the objective, not the whole chord length.

A multi-round optimization strategy [33] is used, resulting in two rounds and total 600 CFD evaluations. The convergence history of the objective functions is plotted in Figure 10. The left shows the best-observed objective function obj , the inverse design objective obj_{inv} , and the direct optimization objective obj_{dir} . The right shows the initial DoE and infill-sampling process. The final optimal point is evaluated, and the comparison of the aerodynamic performance with the baseline airfoil is shown in Table 3. The drag reduction is 32.1 drag counts, and more than 59% laminar flow region on the upper surface is achieved with all of the constraints being satisfied.

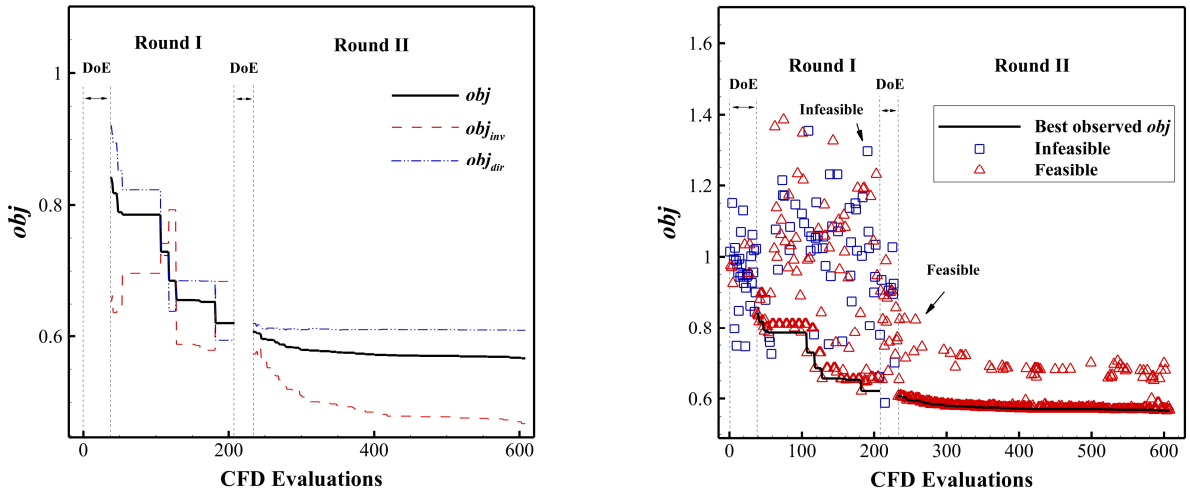

Figure 10 – Convergence history of the hybrid/optimization design of transonic NLF airfoil (left: best-observed obj, obj_{inv} and obj_{dir}; right: initial DoE and infill-sampling)

Table 3 – Comparison of the geometry and aerodynamic performance of the optimal airfoil with the baseline airfoil at the flow condition of $Ma = 0.72,\ Re_c = 2.0\times10^7,\ c_l = 0.6$

Airfoil	c_l	c_d (cts)	c_{df} (cts)	c_l/c_d	c_m	Transition location	t/c
Baseline	0.60	84.6	50.3	70.92	-0.124	Upper surface: 4%	12.7%
Optimum	0.60	52.5	35.0	114.29	-0.112	Upper surface: 59%	12.9%
Δ	0	-32.1	-15.3	43.37	0.012	55%	0.2%

The pressure distributions of the optimal and baseline airfoil are plotted in Figure 11. It can be seen that the optimal pressure distribution shows a rapid acceleration and a small region of adverse pressure gradient at the leading edge, which is beneficial to stabilize the CFI. The strength of the shock wave is also reduced by optimization. The nondimensionalized CFPG of the baseline and optimal airfoil are compared with the inverse design objective, as shown in Figure 12. The nondimensionalized CFPG of the optimal airfoil is in agreement with the objective, especially at the leading edge, which motivates the behaviour of the pressure distribution. However, it has to say that the designed nondimensionalized CFPG is not tightly coincident with the objective. One of the possible reasons is that the weight coefficient of the inverse design objective is relatively small. Another possible reason is that the objective nondimensionalized CFPG is obtained by setting up a minimal equivalent sweep angle (only 10 deg). If it is possible to be coincident with such an objective is not sure merely via modifying the pressure distribution. As a result, it is still an open question, as well as the selecting of the weight coefficient.

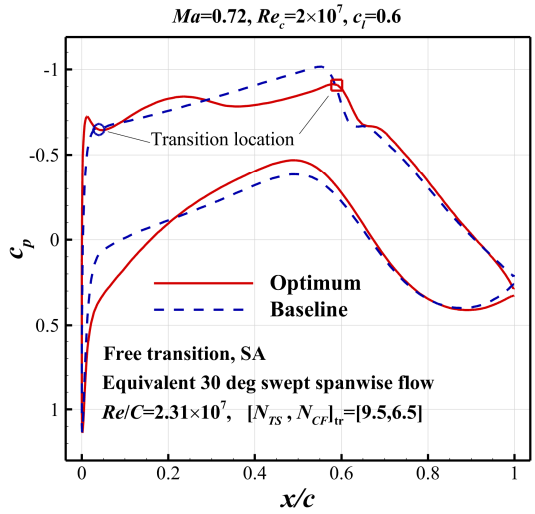

Figure 11 – Comparison of pressure distributions of the optimal airfoil with the baseline airfoil

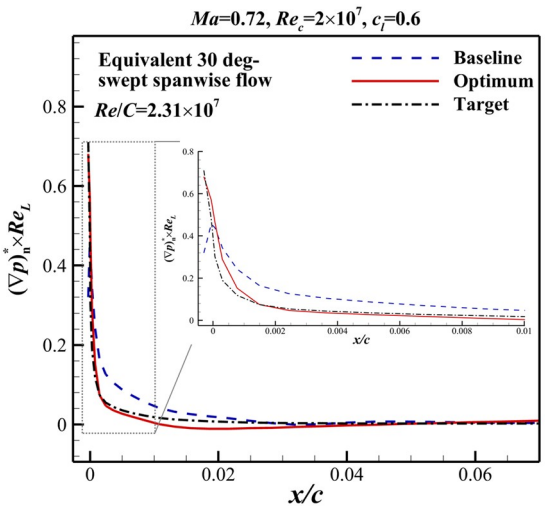

Figure 12 – Comparison of the nondimensionalized CFPG of the baseline and optimal airfoil with the inverse design objective

To validate the effects of the proposed method on suppressing CFI, the amplification N factors of CFI, N_{CF}, are depicted in Figure 13. It can be seen that the N_{CF} of the baseline airfoil exceeds the critical value near the leading edge, while the CFI on the optimal airfoil has been overall suppressed. The amplification N factors of TSI, N_{TS}, as shown in Figure 14, indicate that the TSI on the optimal airfoil is not amplified too much, which is far away from the critical value $\left[N_{TS}\right]_{tr}=9.5$. Because none of the N_{TS} or N_{CF} exceeds the critical value, the laminar flow is regarded as extending to the shock wave location on the upper surface of the optimal airfoil.

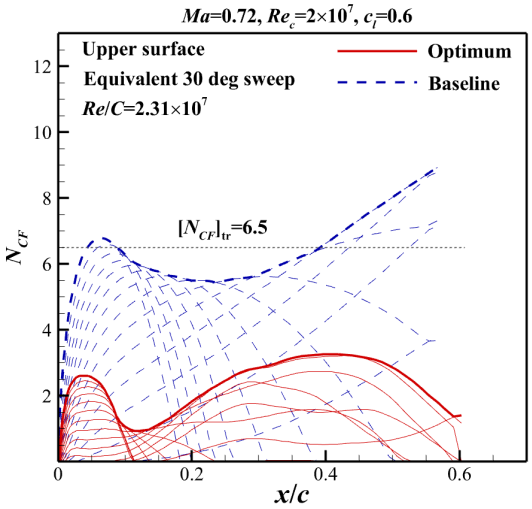

Figure 13 – Amplification N factors of the CFI on the upper surface of the baseline and optimal airfoil

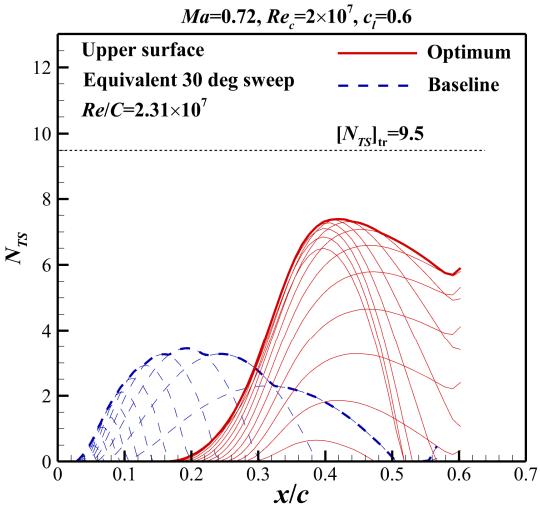

Figure 14 - Amplification N factors of the TSI on the upper surface of the baseline and optimal airfoil

4. Conclusion

In the present paper, a novel design optimization method for transonic NLF airfoils was proposed, allowing for suppressing CFI in the corresponding 3-D case via the nondimensionalized CFPG. The proposed method was validated by the aerodynamic shape optimization for a transonic NLF airfoil

with drag reduction and laminar flow extension objectives. A RANS flow solver featuring automatic transition prediction using the linear stability analysis and the dual e^N method for TSI and CFI was employed to simulate the aerodynamic performance of the airfoils. A hybrid inverse/optimization design method within a surrogate-based optimization framework was used to solve the optimization problem.

A feasible way to set up the inverse design objective of nondimensionalized CFPG was given, making use of its characteristics. The evaluated results show that significant drag reduction and extensive laminar flow on the upper surface were achieved. It was shown that the main driver to extend laminar flow is the overall suppression of the CFI on the upper surface. The feasibility of the proposed method to consider CFI suppression in the corresponding 3-D case using the nondimensionalized CFPG in the design optimization of transonic NLF airfoils was validated.

Beyond the scope of this work, more research should be conducted in the future, such as determining the weight coefficients for the inverse design objective and the direct optimization objective, and the optimization study for a tapped transonic wing and even a supersonic wing.

5. Acknowledgement

This research was supported by the National Natural Science Foundation of China grant No. 11972305, the National Numerical Wind Tunnel Projects No.2019ZT6-A12 and No.2018-ZT1A03, and the “111” project of China No. B17037.

6. Contact Author Email Address

Zhong-Hua Han*, Professor, hanzh@nwpu.edu.cn, Corresponding author.

7. Copyright Statement

References

[1] Reed, H., and Saric, W. Transition Mechanisms for Transport Aircraft. *The 38th Fluid Dynamics Conference and Exhibit*, Seattle, Washington, 2008.

[2] Redeker G, Horstmann K H, Koster H, and Quast A. Investigations on High Reynolds Number Laminar Flow Airfoils. *Journal of Aircraft*, Vol. 25, No. 7, pp. 583–590, 1988.

[3] Campbell R L, and Lynde M N. Natural Laminar Flow Design for Wings with Moderate Sweep. *The 34th AIAA Applied Aerodynamics Conference*, Washington, D.C., 2016.

[4] Ueda Y, Yoshida K, Matsushima K, and Ishikawa H. Supersonic Natural-Laminar-Flow Wing-Design Concept at High-Reynolds-Number Conditions. *AIAA Journal*, Vol. 52, No. 6, pp. 1294–1306, 2014.

[5] Streit T, Wichmann G, zu Hatzbach F von K, and Campbell R L. Implications of Conical Flow for Laminar Wing Design and Analysis. *The 29th AIAA Applied Aerodynamics Conference*, Honolulu, HI, 2011.

[6] Xu Z M, Han Z H, Chi J B, Zhu Z, Song W P. Crossflow Instability Analysis for Swept Natural Laminar Flow Wings Using Nondimensionalized Crossflow Pressure Gradient, *AIAA Journal*, Vol. , No. , pp. , 2021. (In publication)

[7] Gopalarathnam A, and Selig M S. Low-Speed Natural-Laminar-Flow Airfoils: Case Study in Inverse Airfoil Design. *Journal of Aircraft*, Vol. 38, No. 1, pp. 57–63, 2001.

[8] Green B E, Whitesides J L, Campbell R L, and Mineck R E. Method for the Constrained Design of Natural Laminar Flow Airfoils. *Journal of aircraft*, Vol. 34, No. 6, pp. 706–712, 1997.

[9] Lynde M N, and Campbell R L. Computational Design and Analysis of a Transonic Natural Laminar Flow Wing for a Wind Tunnel Model. *The 35th AIAA Applied Aerodynamics Conference*, Denver, CO, 2017.

[10] Ishikawa H, Ohira O, Ohira Y, Matsushima K, and Yoshida K. Development of Supersonic Natural Laminar Flow Wing Design System Using CFD-Based Inverse Method. *The 28th Congress of the International Council of the Aeronautical Sciences*, Brisbane, Australia, 2012.

[11] Amoignon O, Pralits J, Hanifi A, Berggren M, and Henningson D. Shape Optimization for Delay of Laminar-Turbulent Transition. *AIAA Journal*, Vol. 44, No. 5, pp. 1009–1024, 2006.

[12] Driver J, and Zingg D W. Numerical Aerodynamic Optimization Incorporating Laminar-Turbulent Transition Prediction. *AIAA Journal*, Vol. 45, No. 8, pp. 1810–1818, 2007.

[13] Lee J D, and Jameson A. Natural-Laminar-Flow Airfoil and Wing Design by Adjoint Method and Automatic Transition Prediction. *The 47th AIAA Aerospace Sciences Meeting including the New Horizons Forum and Aerospace Exposition*, Orlando, Florida, 2009.

[14] Rashad R, and Zingg D W. Aerodynamic Shape Optimization for Natural Laminar Flow Using a Discrete-Adjoint Approach. *AIAA Journal*, Vol. 54, No. 11, pp. 3321–3337, 2016.

[15] Shi Y, Mader C A, He S, Halila G L O, and Martins J R R A. Natural Laminar-Flow Airfoil Optimization Design Using a Discrete Adjoint Approach. *AIAA Journal*, Vol. 58, No. 11, pp. 4702–4722, 2020.

[16] Halila G L, Martins J R, and Fidkowski K J. Adjoint-Based Aerodynamic Shape Optimization Including Transition to Turbulence Effects. *Aerospace Science and Technology*, Vol. 107, pp. 106243, 2020.

[17] Khayatzadeh P, and Nadarajah S. Aerodynamic Shape Optimization of Natural Laminar Flow (NLF) Airfoils. *The 50th AIAA Aerospace Sciences Meeting including the New Horizons Forum and Aerospace Exposition*, Nashville, Tennessee, 2012.

[18] Han Z H, Chen J, Zhang K S, Xu Z M, Zhu Z, and Song W P. Aerodynamic Shape Optimization of Natural-Laminar-Flow Wing Using Surrogate-Based Approach. *AIAA Journal*, Vol. 56, No. 7, pp. 2579–2593, 2018.

[19] Han Z H, Deng J, and Liu J. Design of Laminar Supercritical Airfoils Based on Navier-Stokes Equations. *The 28th Congress of the International Council of the Aeronautical Sciences*, Brisbane, Australia, 2012.

[20] Zhang Y, Fang X, Chen H, Fu S, Duan Z, and Zhang Y. Supercritical Natural Laminar Flow Airfoil Optimization for Regional Aircraft Wing Design. *Aerospace Science and Technology*, Vol. 43, pp. 152–164, 2015.

[21] Li J, Bouhlel M A, and Martins J R R A. Data-Based Approach for Fast Airfoil Analysis and Optimization. *AIAA Journal*, Vol. 57, No. 2, pp. 581–596, 2019.

[22] Chen J, Song W P, Zhu Z, Xu Z M, and Han Z H. A hybrid inverse/direct optimization design method for transonic laminar flow airfoil. *Acta Aeronautica et Astronautica Sinica*, Vol. 39, No. 12, 2018. (In Chinese)

[23] Chi J B, Han Z H, Fan T L, Zhu Z, and Song W P. Hybrid Inverse/Optimization Design Approach for Transonic Natural-Laminar-Flow Airfoils. *The AIAA Scitech 2019 Forum*, San Diego, California, 2019.

[24] Han S Q, Song W P, Han Z H, Li S B, and Lin Y F. Hybrid Inverse/Optimization Design Method for Rigid Coaxial Rotor Airfoils Considering Reverse Flow. *Aerospace Science and Technology*, Vol. 95, pp.

105488, 2019.

[25] Sewall W G, McGhee R J, Hahne D E, and Jordan Jr F L. Wind Tunnel Results of the High-Speed NLF (1)-0213 Airfoil. Research in Natural Laminar Flow and Laminar Flow Control, pp. 697–726, 1987.

[26] Saric W S, Reed H L, and White E B. Stability and Transition of Three-Dimensional Boundary Layers. *Annual review of fluid mechanics*, Vol. 35, No. 1, pp. 413–440, 2003.

[27] Han Z H. SurroOpt: A Generic Surrogate-Based Optimization Code for Aerodynamic and Multidisciplinary Design. *The 30th Congress of the International Council of the Aeronautical Sciences*, Daejeon, Korea, 2016.

[28] Han Z H. Kriging Surrogate Model and Its Application to Design Optimization: A Review of Recent Progress. *Acta Aeronautica et Astronautica Sinica*, Vol. 37, No. 11, pp. 3197–3225, 2016. (In Chinese)

[29] Han Z H, Xu C Z, Qiao J L, Liu F, Chi J B, Meng G Y, Zhang K S, and Song W P. Recent Progress of Efficient Global Aerodynamic Shape Optimization Using Surrogate-Based Approach. *Acta Aeronautica et Astronautica Sinica*, Vol. 41, No. 5, 2020. (In Chinese)

[30] Han Z H, Xu C Z, Zhang L, Zhang Y, Zhang K S, and Song W P. Efficient Aerodynamic Shape Optimization Using Variable-Fidelity Surrogate Models and Multilevel Computational Grids. *Chinese Journal of Aeronautics*, Vol. 33, No. 1, pp. 31-47, 2020.

[31] Zhang K S, Han Z H, Gao Z J, and Wang Y. Constraint Aggregation for Large Number of Constraints in Wing Surrogate-Based Optimization. *Structural and Multidisciplinary Optimization*, Vol. 59, No. 2, pp. 421-438, 2019.

[32] Roy C J. Grid Convergence Error Analysis for Mixed-Order Numerical Schemes. *AIAA Journal*, Vol. 41, No. 4, pp. 595–604, 2003.

[33] Han Z H, Zhang Y, Xu C Z, Wang K, Wu M M, Zhu Z, and Song W P. Aerodynamic Optimization Design of Large Civil Aircraft Wings Using Surrogate-Based Model. Acta Aeronautica et Astronautica Sinica, Vol. 40, No. 1, 2019. (In Chinese)